Single-cell mass cytometry of TCR signaling: Amplification of small initial differences results in low ERK activation in NOD mice

Michael Mingueneau[a,1], Smita Krishnaswamy[b], Matthew H. Spitzer[c], Sean C. Bendall[c], Erica L. Stone[d], Stephen M. Hedrick[d], Dana Pe'er[b], Diane Mathis[a,2], Garry P. Nolan[c], and Christophe Benoist[a,2]

[a]Division of Immunology, Department of Microbiology and Immunobiology, Harvard Medical School, Boston, MA 02115; [b]Department of Biological Sciences, Columbia Initiative for Systems Biology, Columbia University, New York, NY 10027; [c]Baxter Laboratory in Stem Cell Biology, Department of Microbiology and Immunology, Stanford University, Stanford, CA 94305; and [d]Molecular Biology Section, Division of Biological Sciences, Department of Cellular and Molecular Medicine, University of California, San Diego, La Jolla, CA 92093

Contributed by Christophe Benoist, October 7, 2014 (sent for review August 27, 2014; reviewed by Leslie J. Berg and Arthur Weiss)

Signaling from the T-cell receptor (TCR) conditions T-cell differentiation and activation, requiring exquisite sensitivity and discrimination. Using mass cytometry, a high-dimensional technique that can probe multiple signaling nodes at the single-cell level, we interrogate TCR signaling dynamics in control C57BL/6 and autoimmunity-prone nonobese diabetic (NOD) mice, which show ineffective ERK activation after TCR triggering. By quantitating signals at multiple steps along the signaling cascade and parsing the phosphorylation level of each node as a function of its predecessors, we show that a small impairment in initial pCD3ζ activation resonates farther down the signaling cascade and results in larger defects in activation of the ERK1/2–S6 and IκBα modules. This nonlinear property of TCR signaling networks, which magnifies small initial differences during signal propagation, also applies in cells from B6 mice activated at different levels of intensity. Impairment in pCD3ζ and pSLP76 is not a feedback consequence of a primary deficiency in ERK activation because no proximal signaling defect was observed in *Erk2* KO T cells. These defects, which were manifest at all stages of T-cell differentiation from early thymic pre-T cells to memory T cells, may condition the imbalanced immunoregulation and tolerance in NOD T cells. More generally, this amplification of small initial differences in signal intensity may explain how T cells discriminate between closely related ligands and adopt strongly delineated cell fates.

CyTOF | signaling | single-cell | NOD | diabetes

Engagement of the T-cell receptor (TCR) by peptides bound to major histocompatibility complex (MHC) molecules conditions virtually all phases of T-cell differentiation and activation. For mature T cells, signals from the TCR engaged by cognate antigenic ligands trigger proliferative expansion and effector differentiation. For immature thymocytes, cell fate decisions depend on signals from self-ligands: positive selection into mature T cells, clonal deletion by apoptotic cell death, or deviation into alternative differentiation pathways, such as NKT or FoxP3$^+$ regulatory T cells (Tregs). Contrasting with these radically different outcomes, these ligands engage the TCR within a narrow range of moderate to low affinity. Signal transduction downstream from the TCR must somehow transform the many similar signals emanating from the TCR into clearly different transcriptional outcomes.

The nonobese diabetic (NOD) mouse model of type 1 diabetes (T1D) is arguably one of the best models of human autoimmune disease, sharing with human T1D strikingly similar genetic determinism and many pathological features. The central role of T cells in T1D is clearly established, consistent with the major impact of the MHC on susceptibility. However, the paths through which the NOD or human genetically susceptible backgrounds lead to a breakdown in the normal barriers of self-tolerance remain poorly understood. In principle, one could hypothesize an increased burden of autoreactive T cells, primary defects in immunoregulatory pathways, such as Tregs, or both. Any of these might result from altered TCR signal transduction.

A primary defect in thymic deletion of autoreactive thymocytes in NOD mice had been suggested by several studies (1–4), but our more recent work (5) showed that the phenotypes observed in TCR transgenics on the NOD background were not caused by a resistance to negative selection but instead, inefficient deviation to the γδT lineage. This phenotype was caused by a selective defect in ERK1/2 activation downstream of the TCR, which is apparently an isolated defect, because calcium mobilization and general phosphotyrosine activation seemed normal in activated NOD T cells (5). This defect in ERK phosphorylation on TCR engagement was recently confirmed by an independent study (6), and it manifests at all stages of T-cell differentiation from early thymic pre-T cells to mature T cells in peripheral organs.

ERK1/2 kinases play a key role in many cell types for cell survival and proliferation (7). Surprisingly, they are not mandatory for either T-cell proliferation or clonal deletion induced by self-recognition (8–11). Because ERK1/2 kinases are strictly required for positive selection into mature thymocytes (9), the ERK deficiency in the NOD T-cell lineage might result in an affinity shift or reduced diversity in the TCR repertoire of

Significance

Activation of T lymphocytes by the rearranged T-cell receptor (TCR) conditions essentially all aspects of their differentiation and function, and variations in the efficacy of signal transduction condition pathogen resistance and autoimmune deviation. We explored the defects in signal transduction downstream of the TCR in diabetes-susceptible nonobese diabetic (NOD) mice using mass cytometry and computational processing of single-cell data. We found that small initial differences in the efficacy of triggering at the apex of the cascade result in much more profound differences downstream, with the system being set to amplify the discriminating power of initial sensing to arrive at more marked response/no response decisions within T cells.

Author contributions: M.M., S.K., M.H.S., S.C.B., E.L.S., S.M.H., D.P., D.M., G.P.N., and C.B. designed research; M.M., M.H.S., S.C.B., and E.L.S. performed research; M.M., M.H.S., S.C.B., E.L.S., S.M.H., D.P., D.M., G.P.N., and C.B. analyzed data; and M.M., S.K., M.H.S., S.C.B., E.L.S., S.M.H., D.P., D.M., G.P.N., and C.B. wrote the paper.

Reviewers: L.J.B., University of Massachusetts Medical Center; and A.W., University of California, San Francisco.

The authors declare no conflict of interest.

[1]Present address: Department of Immunology, Biogen Idec, Cambridge, MA 02142.

[2]To whom correspondence should be addressed. Email: cbdm@hms.harvard.edu.

This article contains supporting information online at www.pnas.org/lookup/suppl/doi:10.1073/pnas.1419337111/-/DCSupplemental.

conventional T cells (Tconvs) and/or Tregs, a prediction that agrees with previous observations (12).

It is, thus, important to understand the molecular origin and consequences of the sluggish ERK activation in NOD T cells. TCR signaling pathways in NOD mice have not been explored with currently available technologies. Early reports suggested a defect in RAS activation in NOD T cells (13), a defect proposed to result from an enhanced association of Fyn with the TCR (14) or an excess of free TCRζ and CD3γε chains on the plasma membrane (15). To define the footprint of NOD genetic variation on TCR signaling networks in a systematic manner, we analyzed the dynamics of the events at 16 different steps of the TCR-induced signaling cascade by multidimensional mass cytometry (16, 17). We applied novel conditional density-based visualization and quantitative edge analyses to assess, at the single-cell level, the transmission of signal between nodes, allowing the quantitative comparison of transduction efficiency at these steps (edges in network terminology). We uncovered mechanisms that explain how amplification of signal discrimination may stem from the emergent properties of the TCR signaling network.

Results

To trace the origin and consequences of the ERK signaling defect in NOD T cells, we took advantage of the multidimensional capabilities of mass cytometry and assessed the phosphorylation status of 16 different nodes of the TCR signaling cascade over time at single-cell resolution. Thymic or lymph node cell suspensions from C57BL/6.H2^{g7} (B6^{g7}) and NOD mice were stimulated simultaneously (biotinylated anti-TCR and -CD28 cross-linked with streptavidin) in the same tube, a key aspect of the protocol that ensured synchrony of responses and largely eliminated most sources of confounding differences between responding cells. At various time points, cells were fixed and stained with 24 metal-conjugated antibodies. These included reagents against nine cell surface markers to distinguish various T-cell subpopulations and against CD45.2 and CD45.1 alleles to distinguish cells from B6^{g7} and NOD origin (Fig. 1*A*). Sixteen antibodies probed the phosphorylation level of key nodes of the pathways triggered by TCR engagement with different kinetics (Fig. 1 *B* and *C*). Overall, the panel probed several major signaling pathways in T cells, including the most proximal signaling nodes (pCD3ζ, pZAP70, pLAT, pSLP76, and pc-CBL), the NF-κB pathway (pNF-κB and IκB total protein levels), the ERK1/2 MAPK pathway (pERK1/2 and pS6), the p38 pathway (pMAPKAPKII), the AKT–mTOR pathway (pAKT, pS6, and p4EBP1), the CREB pathway (pCREB), and the integrin pathway (pFAK) (Fig. 1*C* and Table S1).

Selective Attenuation of TCR Signaling in NOD Mice. We first compared phosphorylation events induced by anti-TCR/CD28 triggering of naïve (CD4$^+$TCRβ$^+$CD25$^-$CD44^{low}) Tconvs from freshly harvested lymph nodes of B6^{g7} and NOD mice (4–5 wk of age when autoimmune activation is still very limited in NOD mice).

The results display graphically the progression of the signal through these different nodes (Fig. 2*A*). Phosphorylation of CD3ζ was the earliest event detected, but it was transient and became almost undetectable after 2 min. Phosphorylation of the downstream SLP76 and LAT adaptor molecules was more sustained but also waned by 3 and 6 min, respectively. In contrast to these proximal nodes, ERK phosphorylation was not detected until 2 min poststimulation. The phosphorylation of S6 ribosomal protein and CREB (two nonexclusive targets of ERK1/2) as well as MAPKAPKII (a p38 target) peaked a little later and was sustained until 20 min. NF-κB and RB showed sustained phosphorylation levels during the entire stimulation without evidence of down-modulation. IκB degradation was not detected until after 20 min poststimulation. Finally, some of the probed signaling nodes gave weak or undetectable signals (pZAP70, pCBL, and pAKT in particular) because of either the weak affinity of the corresponding antibodies or the low target abundance in these conditions (clear phosphorylation was detected for all of these phosphoproteins when cells were stimulated with anti-CD3/CD28/CD4 antibodies) (Fig. 2*C*).

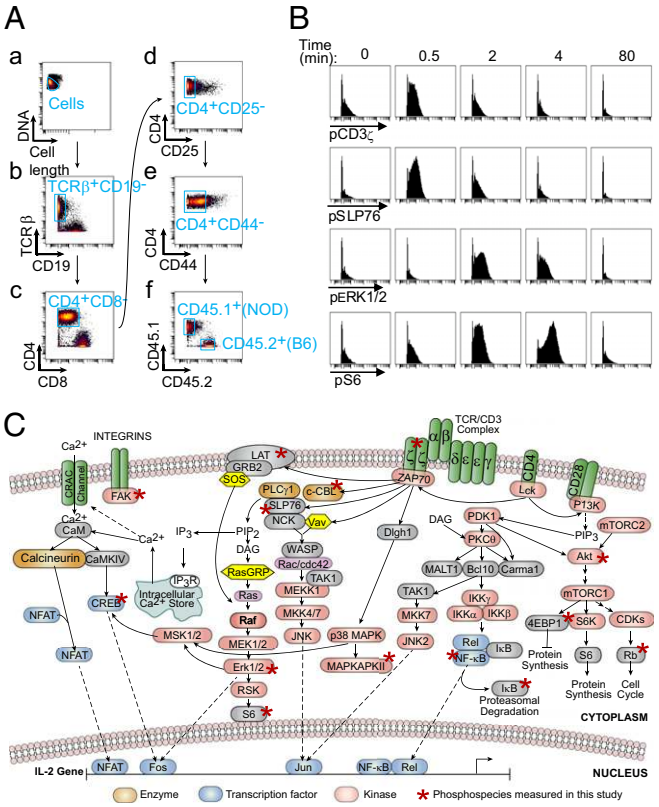

Fig. 1. Analysis of TCR-induced phosphospecies by mass cytometry. (*A*) Sequential gating strategy used to analyze signaling events in naïve B6^{g7} and NOD CD4$^+$ T cells (*a*–*f*). Cells are identified as DNA$^+$ events. (*B*) Typical phosphorylation levels detected for CD3ζ, SLP76, ERK1/2, and S6 in CD4$^+$ T cells from B6^{g7} mice at various time points (CD3ε + CD28 cross-linking). (*C*) Major signaling pathways downstream of the TCR. *Phosphospecies measured in this study.

Relative to B6^{g7}, T cells from NOD mice did not show major differences in the dynamics of signaling (Fig. 2*A*), but quantitative differences were clear, including slightly decreased phosphorylation levels of CD3ζ and SLP76, a more pronounced decrease in the phosphorylation of the ERK1/2–S6–CREB–MAPKAPK2 signaling module, and an impaired degradation of IκBα at late time points poststimulation. In contrast, other signaling nodes (p-LAT, p-FAK, NF-κB, PARP, and RB) seemed less affected by NOD genetic variation. To quantify these differences, these stimulation experiments were repeated with seven independent pairs of B6^{g7} and NOD mice, and the phosphorylation differential between the two genetic backgrounds was averaged (Fig. 2*B*). These differences were reproducible and significant across independent stimulation series: pCD3ζ at 30 s, $P = 0.003$; pSLP76 at 1 min, $P = 0.0007$; pERK1/2 at 2 min, $P = 0.0006$; pS6, pCREB, and pMAPKAPK2 at 3 min, $P = 0.001$, $P = 0.003$, and $P = 0.001$, respectively; IκBα at 20 min, $P = 0.001$ (t test). The differences in pCD3ζ abundance were small but consistent (Fig. 2 *B* and *D*); this decreased phosphorylation did not result from a difference in total CD3ζ between B6^{g7} and NOD T cells (Fig. S1), which is in accordance with the work by Lundholm et al. (18). We conducted a control experiment with cells from B6 (CD45.2) and B6.CD45.1 congenic mice to evaluate the contribution of technical variation. The phosphorylation differential detected between genetically identical mice was minimal (Fig. S2), confirming that the variations did reflect true differences in TCR signaling networks.

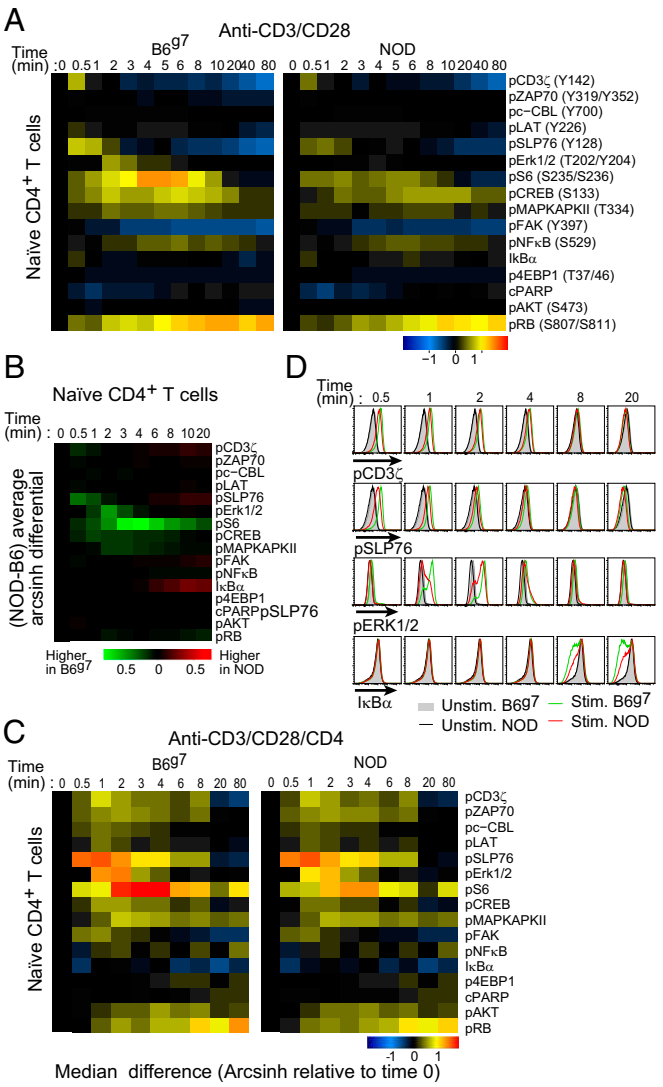

Fig. 2. Analysis of TCR signaling events at the population level identifies selectively attenuated modules in NOD mice. (*A*) Induced phosphorylation levels of indicated signaling molecules at different time points after cross-linking of CD3ε and CD28 in naïve CD4$^+$ T cells from B6^{g7} and NOD mice. Phosphorylation levels were calculated as the difference between the inverse hyperbolic sine (arcsinh) of the median signal intensity at any time point and the arcsinh of the median signal intensity in unstimulated conditions. Representative of seven independent series. (*B*) Differential phosphorylation between B6^{g7} and NOD activated T cells averaged across seven independent series. (*C*) The same as in *A* but after cross-linking of CD3ε, CD28, and CD4. Representative of three independent series. (*D*) Histograms depicting phosphorylation levels detected by conventional flow cytometry after activation of CD4$^+$ T cells from B6^{g7} (green) and NOD (red) mice (CD3ε + CD28 cross-linking). Representative of six independent series.

To determine if these selective signaling defects in NOD Tconvs could be compensated for by increased signal strength, we repeated this experiment in the presence of anti-CD4 in addition to anti-CD3 and -CD28. As expected, the recruitment of CD4 coreceptors in the vicinity of TCR and CD28 costimulatory molecules led to enhanced and more sustained signaling events in both B6^{g7} and NOD Tconvs (Fig. 2*C*). The selective attenuation in the phosphorylation of SLP76 and ERK1/2–S6–CREB and the impaired degradation of IκBα previously seen in NOD T cells were again observed but more muted than without CD4 (about 50% of the reduction seen in anti-CD3/28–stimulated cells). These differences were also present in T cells from BDC2.5 TCR tg mice (19), in which the TCR repertoire is restricted (Fig. S3). Therefore, these differences reflected intrinsic properties of NOD TCR signaling networks, irrespective of the TCR specificity. To bolster these mass cytometry results, we confirmed with fluorochrome-conjugated antibodies the differences in the phosphorylation of CD3ζ, SLP76, ERK1/2, and S6 and the total levels of IκBα (Fig. 2*D* and Fig. S4).

Impact of NOD Genetic Variation at the Single-Cell Level. Mass cytometry informs on signaling events at the single-cell level, which can potentially shed light on novel signaling mechanisms by exploiting the natural variation in signal intensity and activation status of signaling nodes in individual cells. Information on how signals are processed and propagated can be inferred by analyzing relationships in a large number of individual cells. To learn pairwise relationships between signaling molecules, we used a conditional density-based method known as conditional density rescaled visualization to visualize directional relationships between molecules (20). After designating the *x* and *y* axes of a graph to represent the log-transformed signal intensity for two molecules, this method partitions the data into thin slices along the *x* axis and calculates a local density on the *y* axis for each slice on the *x* axis (Fig. 3*A*). Then, the visual is rendered slice by slice by coloring with the corresponding conditional density and smoothing. The signaling relationships generally took a sigmoidal form, with information in both the shapes of the sigmoid and its inflection points as illustrated, for example, for the pCD3ζ–pSLP76 connection (edge) in Fig. 3*B*. This

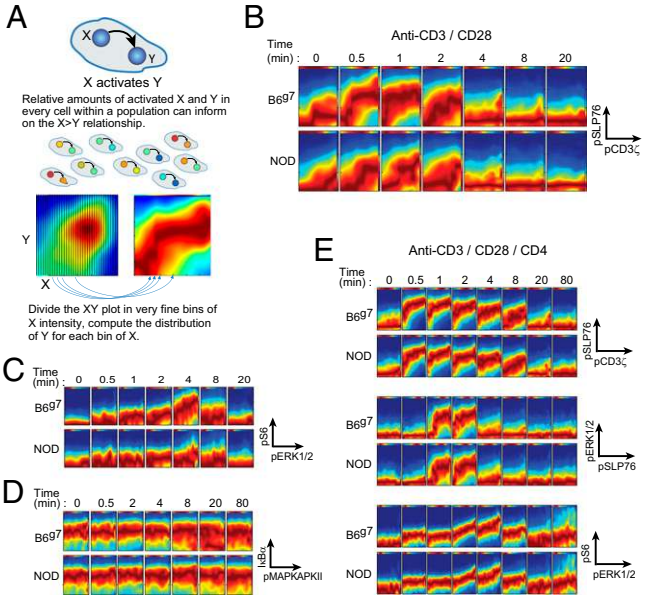

Fig. 3. Conditional density-based analysis of phosphospecies in single cells reveals different signaling relationships in B6^{g7} and NOD T cells. (*A*) Conditional density-based density rescaled visualization method used to visualize relationships between signaling molecules in every cell within a population. The method conditions on thin slices of the *x* axis and computes the conditional density of the *y*-axis molecule for each slice on the *x* axis. The visual is then rendered slice by slice by coloring with the corresponding conditional density and smoothing. This visualization method describes how the *y*-axis molecule changes as a function of the *x*-axis molecule. (*B*–*D*) Conditional density visualization of the relationship between (*B*) pCD3ζ and pSLP76, (*C*) pERK1/2 and pS6, and (*D*) pMAPKAPKII and IκB in naïve CD4$^+$ T cells from B6^{g7} and NOD (CD3ε + CD28 cross-linking). Representative of four independent series. (*E*) Visualization of the relationships between (*Top*) pCD3ζ and pSLP76, (*Middle*) pSLP76 and pERK1/2, and (*Bottom*) pERK1/2 and pS6 in CD4$^+$ T cells from B6^{g7} and NOD mice (CD3ε + CD28 + CD4 cross-linking). Representative of three independent series.

relationship was activated very quickly after stimulation (0.5 min) in T cells from B6^{g7} mice, with a sharp transition between low and high pSLP76 at a value of pCD3ζ between 0.5 and 1 min revealing a digital type of response. It was maintained for several minutes but with a clear shift in the inflection point: lower levels of pCD3ζ were required for a transition to high pSLP76 at 1 min but then, were shifted back to higher levels, perhaps indicating that a negative control element (e.g., a phosphatase such as CD45, PTPN22, or SHP-1) (21) comes into play extremely quickly to dampen SLP76 activation by the pCD3ζ–ZAP70 complex. These curves had similar shapes for NOD T cells but were shifted to the right, indicating that the threshold value of CD3ζ phosphorylation required for maximal phosphorylation of SLP76 was higher. Thus, the main difference between T cells of the two strains was the relationship between pCD3ζ and pSLP76 rather than the actual abundance of total or phosphorylated CD3ζ subunits. Interestingly, the pCD3ζ–pSLP76 edge differed between NOD and B6^{g7} T cells not only after TCR stimulation but also, in unstimulated cells, suggesting that the trophic MHC–TCR tickling is also affected in NOD T cells. Therefore, this method allowed us to detect subtle differences in the relationships between activated signaling intermediates with overall abundances that were not very different when averaged at the population level.

In contrast, the pERK1/2–pS6 edge was nearly linear at the peak (~4 min) (Fig. 3*C*) without signs of a digital jump in pS6 or a plateau across the operational range of pERK1/2. In T cells from NOD mice, this edge was less active and did not reach the levels of pS6 observed in B6^{g7} T cells, even at equivalent levels of ERK1/2 phosphorylation.

The pMAPKAPKII–IκBα edge was not active until later time points (10–20 min), and it showed a clear digital behavior with two distinct states (IκBα^{high} and IκBα^{low} states) (Fig. 3*D*), consistent with conventional cytometry data (Fig. 2*D*). This negative relationship showed that a decrease in IκBα protein (resulting from proteolytic degradation) was only observed beyond a certain level of upstream signaling, which was assessed here by MAPKAPKII phosphorylation. This curve was shifted to the right in T cells from NOD mice, and a smaller fraction of cells from the NOD strain reached the IκBα^{low} state.

The same conditional density plots were generated for cells stimulated with the stronger anti-CD3/CD28/CD4 combination (Fig. 3*E*). The phosphorylation of both SLP76 and ERK1/2 showed a largely digital behavior, which was indicated by the shapes of the pCD3ζ–pSLP76 and pSLP76–pERK1/2 edges and is in accordance with earlier reports (22–25). The marked differences between B6^{g7} and NOD T cells largely disappeared under these strong stimulation conditions, indicating that the strength of upstream signals affects the conditional relationship between downstream signaling nodes.

Relationships Between the Observed Defects in NOD T Cells. As noted above, small but consistent differences in the abundance of pCD3ζ species were detected in T cells from B6^{g7} and NOD mice. The differences in phosphospecies abundances tended to increase along the TCR signaling cascade, with less than a 10% difference in pCD3ζ translating into a 15% difference in pSLP76, a 40% difference in pERK1/2, and an almost 60% difference in pS6 (Fig. 4*A*). We, thus, analyzed the possibility that small initial differences in the phosphorylation of CD3ζ chains might contribute to downstream phosphorylation defects, using the edge activity metric that was developed in ref. 20, which extracts the values of peak density (Fig. 4*B*, red) for each *x* slice of the density plots and averaging them. These values were interpolated to create a smooth curve for each edge, and this curve was integrated to obtain the area under the curve, which is a measure of total kinetic edge activity. The area under the curve metric revealed that the small difference in overall abundance of pCD3ζ in T cells from NOD mice actually translated into a much larger difference in pSLP76, because the signal was passed to pSLP76 through an edge with much lower activity (47% lower) at

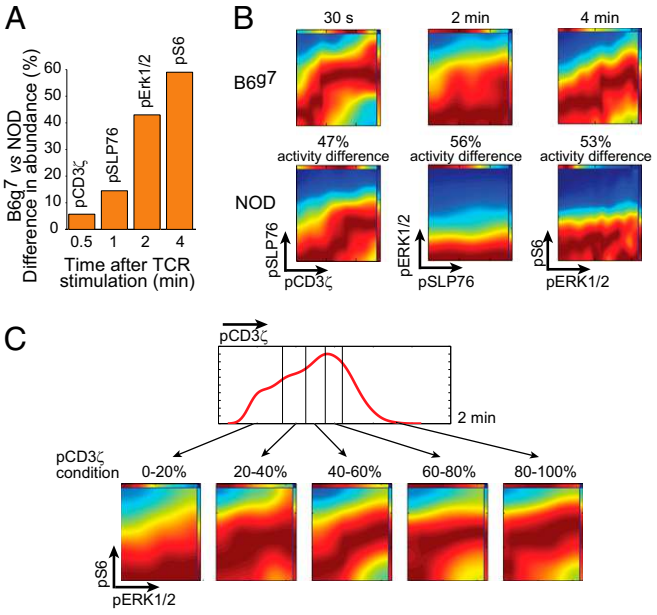

Fig. 4. Amplification of small initial differences in CD3ζ phosphorylation along the signaling cascade in NOD T cells. (*A*) Differences in phosphospecies abundance in activated B6^{g7} and NOD T cells at the peak of phosphorylation. (*B*) Conditional density analysis of the relationship between (*Left*) pCD3ζ and pSLP76, (*Center*) pSLP76 and pERK1/2, and (*Right*) pERK1/2 and pS6 in naïve CD4$^+$ T cells from B6^{g7} and NOD mice at the peak of activity of the corresponding edges after cross-linking of CD3ε and CD28. The difference in edge activity between B6^{g7} and NOD mice is indicated (*SI Methods*) (the edge activity metric is a measure of the area under the curve for the edge response function). (*C*) Analysis of the pERK1/2–pS6 edge conditioned on various levels of pCD3ζ in activated B6^{g7} T cells (CD3ε + CD28 cross-linking). Conditional density plots for the pERK1/2–pS6 edge are shown for cells grouped into five bins based on their levels of pCD3ζ. All representative of four independent series.

the single-cell level. This trend continued, with decreased activity of downstream pSLP76–pERK1/2 (56% lower activity) and pERK1/2–pS6 edges (53% lower activity) (Fig. 4*B*). Therefore, amplification of the differences occurred, because the small difference in the pCD3ζ level was translated into larger differences when passed through differentially active edges along the signaling chain, resulting in the strongly impaired phosphorylation of ERK1/2 and S6 kinase.

To test this hypothesis, we conditioned the analysis of the pSLP76–pERK1/2 edge on various levels of pCD3ζ in T cells from B6^{g7} mice: should the lower level of pCD3ζ in NOD T cells lead to decreased activity of downstream edges, selecting B6^{g7} T cells with varied levels of pCD3ζ would reproduce the same downstream effects. The cell population at 2 min was divided into five bins based on levels of pCD3ζ (Fig. 4*C*, *Upper*), and conditional intensity in the pERK1/2–pS6 edge was computed for each bin. In accordance with our hypothesis, cells with lower pCD3ζ levels had less active pERK1/2–pS6 edges manifested by a shift of the density curve toward the right, indicating that higher levels of pERK1/2 were required to reach the same levels of pS6 (Fig. 4*C*). Even a 20% decrease in pCD3ζ abundance led to a marked reduction in pERK1/2–pS6 edge activity. Thus, the relationship between the intensity of the triggering pCD3ζ and the conditional activity of downstream edges also applies in the reference mouse strain.

Another explanation for the spread of differential activation in NOD T cells might be that a primary defect in ERK activation exists and dampens (through less efficient positive feedback) the activation of earlier steps in the TCR response cascade. To test this hypothesis, we compared T-cell activation in *Erk2*-sufficient B6.CD45.1 and *Erk2*-deficient B6.CD45.2.*Erk2*$^{fl/fl}$.CreERT2$^+$

mice. *Erk2*-deficient T cells showed the expected decrease in pERK1/2, pS6, and to a lower extent, pMAPKAPK2 (Fig. 5). However, the activation of all proximal TCR signaling nodes (pCD3 and pSLP76) was intact, and there was no difference in total IκBα levels (Fig. 5). Thus, the initial differences in pCD3ζ and pSLP76 are truly attributable to NOD genetic variation and not an indirect effect of the *Erk2* deficiency.

CD4SP thymocytes, $CD44^{hi}$ effector/memory $CD4^+$ T cells, and $CD25^+$ $CD4^+$ Tregs showed the same $B6^{g7}$ vs. NOD differential of the ERK1/2–S6–CREB signaling module and a more subtle difference in pCD3ζ (Fig. S5*A*). These defects were also observed in polyclonal DP thymocytes and BDC2.5 TCR tg DP thymocytes on stimulation with anti-CD3/28/4 (Fig. S5*B*), albeit with a stronger differential on pCREB than on pS6. When activated more physiologically by A^{g7} MHC tetramers loaded with BDC2.5 agonist peptide (Fig. S5*C*), DP thymocytes showed similar defects.

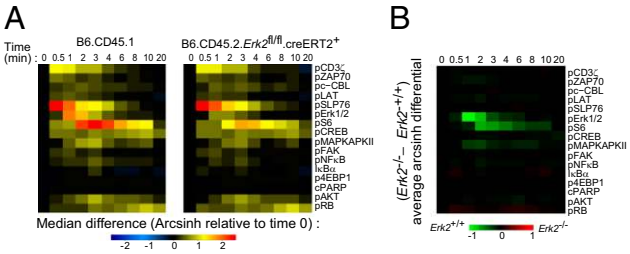

Fig. 5. Mass cytometry analysis of T-cell activation in genetically *Erk*-deficient T cells. (*A*) Induced phosphorylation levels after CD3ε + CD28 cross-linking in $CD4^+$ T cells from (*Left*) tamoxifen-treated *Erk2*-sufficient B6.CD45.1 and (*Right*) *Erk2*-deficient B6.CD45.2.$Erk2^{fl/fl}$.CreERT2$^+$ mice. (*B*) Phosphorylation differential between *Erk2*-deficient and -sufficient mice averaged across two independent series.

Discussion

This application of mass cytometry shows a dynamic map of TCR-induced phosphospecies in T cells and their genetic variation at an unprecedented resolution. This experimental strategy offers several advantages compared with the more conventional immunoblot or fluorescence-based detection of phosphorylation events. (*i*) This approach is highly multiparametric, allowing for the simultaneous detection of up to 36 molecular species, and it should allow up to 100 metal masses, with future developments of new antibody reagents and metal conjugation chemistries. (*ii*) Mass cytometry allows the direct comparison of multiple cell subsets within the same heterogeneous sample; the robustness of our results relies on mixing cells of the two strains in the same tube and eschewing technical variations, which are nontrivial for such rapid responses. One caveat to our study is that the perspective is limited to the phosphorylation events for which flow compatible antibodies are available, which may miss some important sites or sites of different functional consequence on a single molecule. (*iii*) The resulting single-cell data bring the possibility to not only analyze signaling events as population averages for a cell type at a given time point but also, computationally extract information from correlated analysis of nodes in individual cells by observing and exploiting the variation and stochasticity in the population.

This exploration was motivated by our prior observation that T cells from NOD mice have a defect in the ERK1/2 signaling module (5). We used a panel of 25 antibodies to probe signaling networks in T cells from NOD mice across 15 time points to determine if this defect in ERK1/2 signaling is the sole node impacted by NOD genetic variation and if not, trace the origin of the defect. This analysis showed that overall TCR signaling dynamics are normal in NOD mice. However, two signaling modules seemed to be strongly affected: the ERK1/2–S6–CREB module, which had components that were less phosphorylated, and IκBα, whose degradation was impaired. Upstream of these pathways, we also noted more subtle reductions in the phosphorylation of pCD3ζ and pSLP76. Activation of other signaling pathways seemed largely unaffected, which is in agreement with the observation that Ca^{2+} signaling is normal in T cells from NOD mice (5). The ERK1/2 and IκBα defects were not directly related, because *Erk2*-deficient T cells recapitulated the defects in ERK1/2 and S6 phosphorylation but not those in IκBα degradation.

Analysis of these data at single-cell resolution by determining the conditional intensity of activation of one node as a function of the activation of its predecessors allowed an integration of these observations by showing the differential activity of several edges along the path from pCD3ζ to pERK–pS6. The edge analysis revealed that the pSLP76–pERK1/2 and pERK1/2–pS6 edges were less active in T cells with lower pCD3ζ activation. It was not simply that cells with lower pCD3ζ had lower pERK1/2 (which would be trivial) but that the relation between pSLP76 and pERK was shifted as a function of pCD3ζ (at an equivalent level of pSLP76, the amount of pERK1/2 generated was lower in cells with low pCD3ζ). Thus, a small difference in signal intensity at the apex of the cascade influenced the efficiency of some of the downstream steps. This observation was true whether comparing $B6^{g7}$ and NOD T cells or across the range of $B6^{g7}$ T cells distinguished as a function of their pCD3ζ levels. In other words, one cannot think of the pSLP76–pERK1/2 edge as an isolated unit that maps levels of pSLP76 to pERK1/2 but must think of it as one with efficacy that is affected by upstream events (in effect, a form of kinetic proofreading). Thus, these observations show that the TCR signal transduction system is distinctly nonlinear, amplifying small differences as it propagates the signal. As proposed previously (26, 27), this property contributes to the exquisite sensitivity of T cells for ligands for which the TCR has only moderate affinity and that need to be discriminated from very similar analogs.

If the defective pERK1/2 and IκBα activations result from subtly lower activation of proximal TCR signaling, why are only some but not all signaling pathways affected in NOD T cells? The mechanisms evoked above may result, depending on the properties of each downstream signaling module, such as their activation threshold or analog/digital behavior, in differential sensitivity to small differences in initial activation. Indeed, T-cell signaling pathways leading to cytokine production and proliferation were reported to be differentially sensitive to immunoreceptor tyrosine-based activation motif (ITAM) multiplicity and differences in proximal signaling (28). The ERK1/2 signaling node functions as a bimodal switch (22–25), and this digital behavior is reflected here. In contrast, the down-stream phosphorylation of S6 seems to be an analog type of response, thus revealing the existence of mechanisms converting digital ERK1/2 signals into downstream analog outputs. Single-cell analysis of IκBα degradation also revealed a digital behavior, which is in agreement with a previous report (29).

The root of impaired pCD3ζ activation and its downstream consequences in NOD mice remains to be identified. The rightward shift of the conditional intensity curve indicated that a higher number of pCD3ζ subunits was required to reach the same level of SLP76 phosphorylation as in $B6^{g7}$ mice. These observations suggest that some CD3ζ subunits may be sequestered or not available to participate in functional signalosomes, a hypothesis in agreement with earlier reports showing that NOD T cells have an excess of free CD3ζ chains on the plasma membrane (15). Alternatively, regulatory phosphatases like PTPN22, which has genetic variants that are linked to several autoimmune diseases (21), could constrain CD3ζ phosphorylation in NOD cells.

ERK kinases are strictly required for thymic positive selection (9), and thymic selection of Tregs is impaired in NOD mice, generating a reduced TCR repertoire diversity (12). This selection defect in NOD mice was recently mapped to the same genetic locus (*Idd9*) that controls the attenuation of the ERK signaling module in NOD T cells (6). Altogether, these observations suggest that the impaired activation of the ERK signaling module and the decreased diversity of the Treg repertoire in

NOD mice are causally linked events. Importantly, the *Idd9* region affords significant protection from spontaneous diabetes and includes several candidate genes that might plausibly affect TCR signaling, particularly *Lck*, which could contribute to the proximal TCR signaling defect. Beyond thymic selection, it remains to be determined if the defect in ERK signaling also affects Treg homeostasis and suppressive functions. Finally, the functional importance of the impaired degradation of IκBα was not explored here, but given the importance of the NF-κB pathway in Tregs (30), it is possible that it may also impact Treg physiology in NOD mice.

In conclusion, applying the unique capability of mass cytometry to the detection of phosphospecies has provided a high-resolution map of signaling events in T cells, uncovering a mode of signal propagation in which small initial differences are selectively magnified in the differential activation of downstream edges and nodes, and identified the subtle footprint of NOD genetic variation on TCR signaling networks.

Methods

Mice. Mice were maintained in specific pathogen free facilities at Harvard Medical School (Protocol 02954). Age-matched 4- to 6-wk-old male $B6^{g7}$ and NOD, BDC2.5 TCR tg mice on B6 and NOD backgrounds (5) were used. *Erk2*$^{fl/fl}$.CreERT2^{+} and CreERT2^{-} littermate controls (11) were injected i.p. with 2 mg tamoxifen every day for 6 d and analyzed 2 d later.

Cell Stimulation. Lymph node or thymus cell suspensions from $B6^{g7}$ and NOD mice were mixed in the same tube, stimulated in medium containing 6 μg/mL biotinylated anti-CD3ε and anti-CD28 stimulatory antibodies, and incubated for 2 min at 37 °C before the addition of 24 μg/mL streptavidin. At various times after cross-linking, the stimulation was stopped by the addition of paraformaldehyde to 2% (wt/vol) (room temperature for 20 min). In some experiments, biotinylated anti-CD4 antibodies were also included in the stimulation mix. For tetramer stimulation, A^{g7}/BDC2.5 tetramers (National Institutes of Health Tetramer Facility) were added to 10 μg/mL.

Detection of Phosphosignaling Events by Flow and Mass Cytometry. PFA-fixed and frozen lymphocyte suspensions were thawed on ice. In some cases, samples were first barcoded using all six stable palladium isotopes as previously described (31). Each barcoded tube contained 20 individual samples and was stained in 300 μL. Single samples of 10^6 cells were stained in 50 μL with a mixture of metal-conjugated antibodies directed against surface and intracellular antigens, prepared, and titrated as described (17) (Table S1) using a two-step procedure. For fluorescent phosphoflow experiments, the same fluorochrome-conjugated antibody clones were used. After acquisition on a CyTOF I (Fluidigm), time series were normalized to internal bead standards (32). Phosphorylation was calculated as the difference between the inverse hyperbolic sine (arcsinh) of the median signal intensity at any time point and the arcsinh of the median signal intensity in unstimulated conditions (cells incubated in medium without antibodies). The arcsinh transformation (17), similar to the biexponential transformation used for flow cytometry data, is standard for mass cytometry and necessitated by the presence of negative data values resulting from background subtraction and the absence of background autofluorescence in mass cytometry. It essentially applies a log scale to large values in the data but preserves linearity near zero.

Computational Analyses of Mass Cytometry Data. Mass cytometry data plots, heat maps, histograms, and fold change analyses were made with software tools available at www.cytobank.org and custom R scripts. The analysis of relationships between signaling molecules used novel computational algorithms (20) detailed in *SI Methods*.

ACKNOWLEDGMENTS. We thank K. Hattori, A. Ortiz-Lopez, N. Asinovski, and C. Katayama for help with mice and antibodies, and M. McGargill for providing *Erk*-deficient cells. We acknowledge NIH Tetramer Core Facility Contract HHSN272201300006C for provision of A^{g7}/BDC2.5 tetramers. This work was supported by National Institutes of Health or the Juvenile Diabetes Foundation Grants R01AI021372 (to S.M.H.), MCB-1149728 (to D.P.), DP2-OD002414-01 (to D.P.), U54CA121852-01A1 (to D.P.), JDRF 4-2007-1057 (to D.M. and C.B.), P01AI05904 (to D.M. and C.B.), R01AI51530 (to D.M. and C.B.), U19AI057229 (to G.P.N.), U19AI100627 (to G.P.N.), U54CA149145 (to G.P.N.), N01-HV-00242 (to G.P.N.), and FDA-BAA-12-00118 (to G.P.N.). M.M. was supported by Human Frontier Science Program Postdoctoral Fellowship HFSP- LT000096, M.H.S. was supported by a George D. Smith Fellowship, S.C.B. was supported by Postdoctoral Fellowship 1K99 GM104148-01, E.L.S. was supported by Postdoctoral Fellowship K01DK095008, and G.P.N. was supported by the Rachford and Carlotta A. Harris Endowed Professorship.

1. Zucchelli S, et al. (2005) Defective central tolerance induction in NOD mice: Genomics and genetics. *Immunity* 22(3):385–396.
2. Choisy-Rossi CM, Holl TM, Pierce MA, Chapman HD, Serreze DV (2004) Enhanced pathogenicity of diabetogenic T cells escaping a non-MHC gene-controlled near death experience. *J Immunol* 173(6):3791–3800.
3. Lesage S, et al. (2002) Failure to censor forbidden clones of CD4 T cells in autoimmune diabetes. *J Exp Med* 196(9):1175–1188.
4. Liston A, et al. (2004) Generalized resistance to thymic deletion in the NOD mouse; a polygenic trait characterized by defective induction of Bim. *Immunity* 21(6):817–830.
5. Mingueneau M, Jiang W, Feuerer M, Mathis D, Benoist C (2012) Thymic negative selection is functional in NOD mice. *J Exp Med* 209(3):623–637.
6. Ferreira C, Palmer D, Blake K, Garden OA, Dyson J (2014) Reduced regulatory T cell diversity in NOD mice is linked to early events in the thymus. *J Immunol* 192(9):4145–4152.
7. Meloche S, Pouysségur J (2007) The ERK1/2 mitogen-activated protein kinase pathway as a master regulator of the G1- to S-phase transition. *Oncogene* 26(22):3227–3239.
8. D'Souza WN, Chang CF, Fischer AM, Li M, Hedrick SM (2008) The Erk2 MAPK regulates CD8 T cell proliferation and survival. *J Immunol* 181(11):7617–7629.
9. Fischer AM, Katayama CD, Pagès G, Pouysségur J, Hedrick SM (2005) The role of erk1 and erk2 in multiple stages of T cell development. *Immunity* 23(4):431–443.
10. McGargill MA, et al. (2009) Cutting edge: Extracellular signal-related kinase is not required for negative selection of developing T cells. *J Immunol* 183(8):4838–4842.
11. Chang CF, et al. (2012) Polar opposites: Erk direction of CD4 T cell subsets. *J Immunol* 189(2):721–731.
12. Ferreira C, et al. (2009) Non-obese diabetic mice select a low-diversity repertoire of natural regulatory T cells. *Proc Natl Acad Sci USA* 106(20):8320–8325.
13. Rapoport MJ, et al. (1999) Defective activation of p21ras in peripheral blood mononuclear cells from patients with insulin dependent diabetes mellitus. *Autoimmunity* 29(2):147–154.
14. Salojin K, et al. (1997) Impaired plasma membrane targeting of Grb2-murine son of sevenless (mSOS) complex and differential activation of the Fyn-T cell receptor (TCR)-zeta-Cbl pathway mediate T cell hyporesponsiveness in autoimmune nonobese diabetic mice. *J Exp Med* 186(6):887–897.
15. Zhang J, Salojin K, Delovitch TL (1998) Sequestration of CD4-associated Lck from the TCR complex may elicit T cell hyporesponsiveness in nonobese diabetic mice. *J Immunol* 160(3):1148–1157.
16. Bandura DR, et al. (2009) Mass cytometry: Technique for real time single cell multitarget immunoassay based on inductively coupled plasma time-of-flight mass spectrometry. *Anal Chem* 81(16):6813–6822.
17. Bendall SC, et al. (2011) Single-cell mass cytometry of differential immune and drug responses across a human hematopoietic continuum. *Science* 332(6030):687–696.
18. Lundholm M, et al. (2010) Variation in the Cd3 zeta (Cd247) gene correlates with altered T cell activation and is associated with autoimmune diabetes. *J Immunol* 184(10):5537–5544.
19. Katz JD, Wang B, Haskins K, Benoist C, Mathis D (1993) Following a diabetogenic T cell from genesis through pathogenesis. *Cell* 74(6):1089–1100.
20. Krishnaswamy S, et al. (2014) Conditional density-based analysis of T-cell signaling in single cell data. *Science,* in press.
21. Stanford SM, Rapini N, Bottini N (2012) Regulation of TCR signalling by tyrosine phosphatases: From immune homeostasis to autoimmunity. *Immunology* 137(1):1–19.
22. Stefanová I, et al. (2003) TCR ligand discrimination is enforced by competing ERK positive and SHP-1 negative feedback pathways. *Nat Immunol* 4(3):248–254.
23. Altan-Bonnet G, Germain RN (2005) Modeling T cell antigen discrimination based on feedback control of digital ERK responses. *PLoS Biol* 3(11):e356.
24. Das J, et al. (2009) Digital signaling and hysteresis characterize ras activation in lymphoid cells. *Cell* 136(2):337–351.
25. Albeck JG, Mills GB, Brugge JS (2013) Frequency-modulated pulses of ERK activity transmit quantitative proliferation signals. *Mol Cell* 49(2):249–261.
26. Davis MM, et al. (2007) T cells as a self-referential, sensory organ. *Annu Rev Immunol* 25:681–695.
27. Fooksman DR, et al. (2010) Functional anatomy of T cell activation and synapse formation. *Annu Rev Immunol* 28:79–105.
28. Guy CS, et al. (2013) Distinct TCR signaling pathways drive proliferation and cytokine production in T cells. *Nat Immunol* 14(3):262–270.
29. Kingeter LM, Paul S, Maynard SK, Cartwright NG, Schaefer BC (2010) Cutting edge: TCR ligation triggers digital activation of NF-kappaB. *J Immunol* 185(8):4520–4524.
30. Oh H, Ghosh S (2013) NF-κB: Roles and regulation in different CD4(+) T-cell subsets. *Immunol Rev* 252(1):41–51.
31. Bodenmiller B, et al. (2012) Multiplexed mass cytometry profiling of cellular states perturbed by small-molecule regulators. *Nat Biotechnol* 30(9):858–867.
32. Finck R, et al. (2013) Normalization of mass cytometry data with bead standards. *Cytometry A* 83(5):483–494.

Supporting Information

Mingueneau et al. 10.1073/pnas.1419337111

SI Methods

Visualization of 2D Relationships. To visualize 2D relationships in single-cell data, we use a recently developed method known as density rescaled visualization (DREVI). DREVI is designed to highlight the shape and spread of two-variable relationships in single-cell data. It depicts the *y* variable as a stochastic function of the *x* variable, despite noise in measurements and uneven coverage along the dynamic range of the *x* variable, by visualizing the conditional probability of the *y* variable given particular *x* values. Compared with an ordinary density estimate, the visualization shows how the *y* axis changes with the *x* axis rather than simply highlighting where the majority of the data is concentrated.

Regression and Activity Metric. The functional activity of the *x*–*y* relationship, as depicted by DREVI, is captured as an edge response function. This function is defined by the regions of high density in DREVI diagrams using a mixed model regression, which selects among four shape options, including (*i*) linear, (*ii*) sigmoidal, (*iii*) double sigmoidal, and (*iv*) freeform. The edge response function is integrated to compute a measure proportional to the total enzymatic activity of the edge. Hence, the activity metric is a measure of the area under the curve for the edge response function.

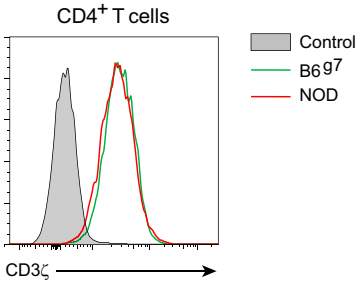

Fig. S1. T cells from B6^{g7} and NOD mice show the same expression levels of CD3ζ. Histograms showing intracellular CD3ζ expression in CD4$^+$ T cells from NOD and B6^{g7} mice. Representative of two independent experiments.

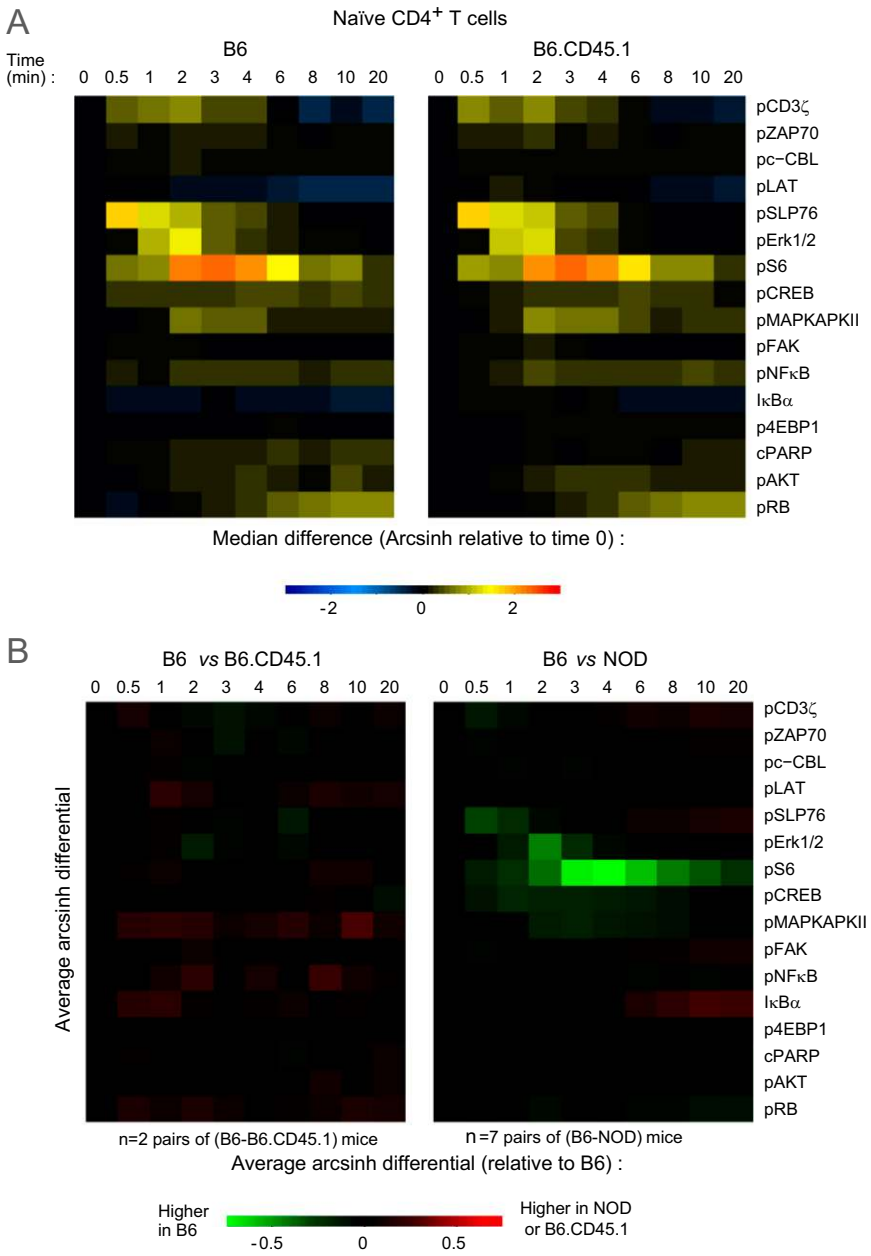

Fig. S2. Validation of the stimulation protocol. Cells from individual mice of the same genetic background signal almost identically when stimulated in the same tube. (*A*) Heat maps showing induced phosphorylation levels of indicated signaling molecules at different time points after cross-linking of CD3ε and CD28 in naïve $CD4^+$ T cells from B6 ($CD45.2^+$) and B6.CD45.1 congenic mice. (*B*) Heat maps depicting the phosphorylation differential (*Left*) between B6.CD45.1 and B6 mice and (*Right*) between $B6^{g7}$ and NOD mice for comparison averaged across two and seven independent stimulation series, respectively.

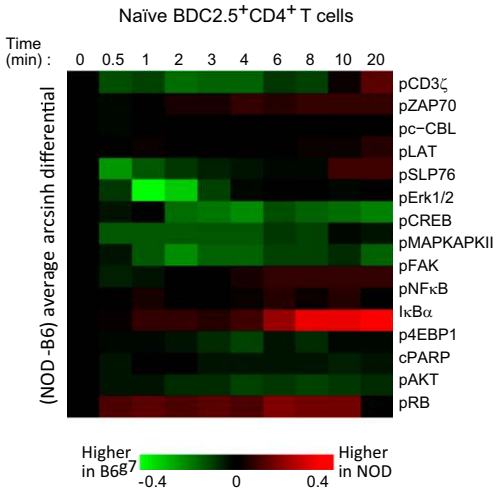

Fig. S3. Signaling defects in NOD mice occur irrespective of TCR specificity. Heat map depicting the phosphorylation differential in naïve $CD4^+$ T cells from NOD and $B6^{g7}$ mice expressing the BDC2.5 tg TCR. Averaged differential calculated across two independent stimulation series.

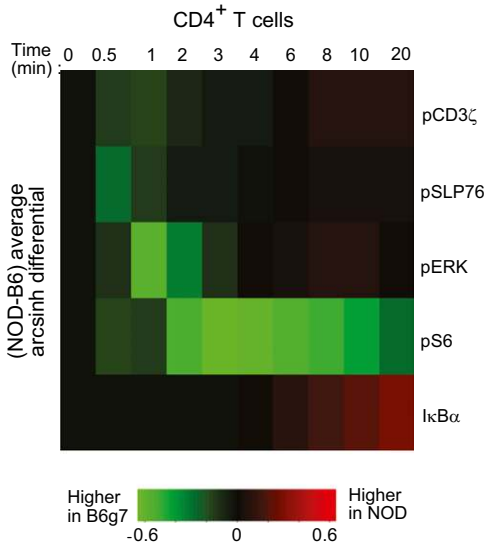

Fig. S4. Validation of mass cytometry results by conventional flow cytometry. Heat map depicting the phosphorylation differential between NOD and $B6^{g7}$ naïve $CD4^+$ T cells corresponding to primary flow cytometry data displayed in Fig. 2*D* and calculated using the same metric as for mass cytometry data [inverse hyperbolic sine (arcsinh) of the median signal intensity]. Averaged differential calculated across six independent stimulation series at various time points after cross-linking of CD3ε and CD28.

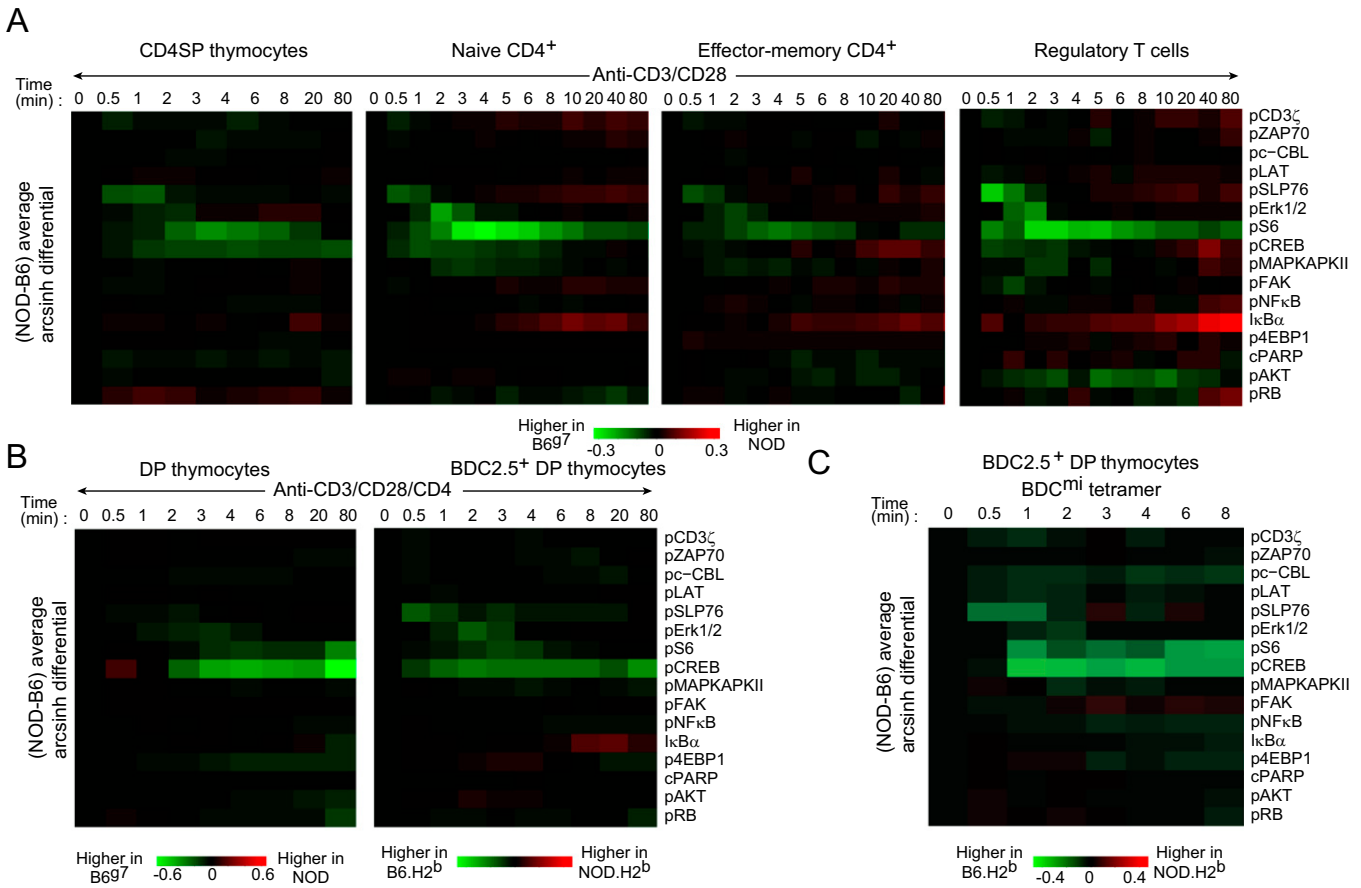

Fig. S5. TCR signaling defects in NOD mice are conserved across differentiation stages and subsets. (*A*–*C*) Heat maps depicting the phosphorylation differential in various T-cell subsets from B6g7 and NOD mice: (*A*) thymic CD4SP thymocytes and peripheral naïve, effector memory, and CD4+ Tregs stimulated with anti-CD3/28 antibodies; (*B*) polyclonal and BDC2.5 TCR tg DP thymocytes stimulated with anti-CD3/28/4 antibodies; and (*C*) BDC2.5 TCR tg DP thymocytes stimulated with Ag7 tetramers loaded with BDC2.5 minotope agonist peptide. Averaged differential calculated from (*A*) four and (*B* and *C*) two independent stimulation series.

Table S1. Cellular antibody staining panel clones, suppliers, isotope reporter, and staining concentration

Target epitope	Clone	Supplier	Isotopic label	Staining concentration (μg/mL or volume/100 μL)
CD45.1	A20	Bio	In113	3
CD45.2	104	Bio	In115	3
Cleaved PARP	F21-852	BD	La139	1
CD5	53–7.3	Bio	Pr141	2
p4EBP1 (T37/46)	236B4	CST	Nd143	3
CD4	RM4-5	DVS	Nd145	1 μL
CD8	53–6.7	DVS	Nd146	1 μL
pFAK (pY397)	Polyclonal	CST	Nd148	3
CD19	6D5	DVS	Sm149	1 μL
Ki67	B56	BD	Sm152	4
pMAPKAPKII (T334)	27B7	CST	Eu153	3
pShp2 (Y580)	Polyclonal	CST	Sm154	2
pSLP76 (Y128)	J141-668.36.58	BD	Gd156	2
pRb (S807/811)	J112-906	BD	Gd158	0.5
pAKT (S473)	D9E	CST	Tb159	4
pSyk/ZAP70 (Y319/Y352)	17a	BD	Gd160	3
pc-CBL (Y700)	47/c-Cbl	BD	Dy162	2
pNF-κB (S529)	K10-895.12.50	BD	Ho165	2
IκBa (N terminus)	L35A5	CST	Er166	3
pErk1/2 (T202/Y204)	197G2	CST	Er167	3
CD25	3C7	BD	Er168	6
TCR-β	H57-597	DVS	Tm169	1 μL
pLAT (Y226)	J96-1238.58.93	BD	Er170	2
CD44	IM7	DVS	Yb171	1 μL
pS6 (S235/236)	N7-548	BD	Yb172	3
pCD3z (Y142)	K25-407.69	BD	Lu175	3
pCreb (S133)	87G3	CST	Yb176	2

All DVS antibodies were purchased preconjugated. All other supplier antibodies were purchased in a carrier-free format and conjugated with the respective metal isotope using the MaxPar-X8 Conjugation Kit (DVS Sciences; in some cases with chloride metal isotopes purchased from Trace Sciences International). BD, BD Biosciences; Bio, Biolegend; CST, Cell Signaling Technologies; DVS, DVS Sciences.